3.16 LES STUDY ON ORGANIZED TURBULENCE STRUCTURES OVER PLANT CANOPIES

Tsutomu Watanabe*
Forestry and Forest Products Research Institute, Tsukuba, Ibaraki, Japan

1. INTRODUCTION

In our experience of tower flux measurements, it is very common to see ramp patterns (i.e., patterns that resemble the teeth of a saw) in time records of scalars (e.g., CO_2, temperature). Through a good deal of field and wind tunnel studies, we learned that ramp patterns are traces of organized turbulence structures which have passed the tower during the recording time, and that a large fraction of the fluxes is driven by such organized structures (for review, see, e.g., Finnigan 2000; Gao et al., 1989; Collineau and Brunet, 1993b; Bergström and Högström, 1989). Therefore, understanding the structure and mechanism of the organized turbulence that causes the ramp patterns is necessary not only for the correct interpretation of measured turbulence data but also for the proper modeling of turbulent transport between plant canopies and the atmosphere.

As discussed by Raupach et al. (1996), canopy flow is distinguished from the surface layer flow by the existence of an elevated (i.e., near the canopy top) inflection point in the vertical profile of the streamwise velocity. The resulting instability mechanism plays a key role in producing active canopy-scale eddies that are supposed to be the main agent for the transport of momentum and scalars across the canopy top. This mixing-layer analogy for canopy turbulence well explains many features of observed statistical flow properties (e.g., large velocity skewnesses; major role of the transport term in TKE budgets; enhanced turbulence diffusivities). Marshall et al. (2002) demonstrated, using wind-tunnel data, that the vertical profiles of mean velocity and velocity variances near forest canopies of different density collapse to a single universal profile when scaled by the basic length scale of the mixing-layer analogy. Katul et al. (1998) argued that active eddy motion, which is shown by the mixing-layer analogy to be the main energy contributor to vertical velocity spectral energy, is also the main contributor to the scalar flux, showing that wavelet cospectra of vertical scalar fluxes peak at a wavenumber that agrees with the prediction by the analogy. These results all indicate importance of the mixing-layer mechanism.

However, actual plant canopies are always under the atmospheric boundary layer in which eddy motions of larger (compared to the canopy height) spatial scales dominate. Since the local wind shear across the canopy top is largely affected by eddy motions in the lower boundary layer, the morphology of canopy turbulence may not be independent of them. Indeed, Katul et al. (1998) found that fluctuations in streamwise velocity and scalar measured over forests include a large contribution made by inactive eddy motions, which are larger-scale eddies not involved directly in the vertical transport across the canopy top. McNaughton and Brunet (2002) suggested, by reviewing previous field measurements, that the inactive and active eddy motions interact with each other. Therefore, in order to reach a complete understanding of turbulence that develops near the canopy – atmosphere interface, we must know the relationship between the canopy-scale eddies produced through the mixing-layer mechanism and the larger-scale eddies originated in the boundary layer.

Many authors indicated the existence of streak structures in the near-surface region of the neutral atmospheric boundary layer, based on numerical simulations (e.g., Deardorff, 1972; Mason and Thomson, 1987; Moeng and Sullivan, 1994; Lin et al., 1996), field measurements (e.g., Wilczak and Tillman, 1980; Drobinski et al., 2004) and theoretical considerations (e.g., Foster, 1997; Drobinski and Foster, 2003). The streaks are elongated regions of low- and high-speed streamwise velocity, which are aligned with the mean wind direction near the surface. The structure of the streaks in the atmospheric boundary layers and the flow patterns associated with them are similar to those of the near-wall streak, which is commonly observed in near-wall shear layers of low Reynolds-number flow (e.g. Robinson, 1991; Panton, 1997). The both streaks develop under the influence of strong shear. The horizontal scale of the atmospheric streaks is typically several hundreds of meters, much larger than the scale of canopies. The flows in these streaks are, therefore, essentially horizontal at the height of canopy tops. In this sense, the effect of streaks may be merely to provide an external condition for the dynamics of canopy turbulence (i.e., gradual variations of mean wind speed). However, the near-surface wind shear which would be enhanced in a region of high-speed streak may give rise to smaller (but still larger than the canopy-scale) eddies above the canopy. These smaller eddies, if they exist, can interact with canopy-scale eddies. From similarity, these eddies may also take a streaky form.

The main goal of the present study is to elucidate the connection between the flux-transporting events (i.e., ramp patterns) and the larger-scale eddy motions produced above the canopy, using large eddy simulations of the neutrally stratified flow within and above an ideally homogeneous plant canopy. The organized turbulence structures that cause ramp patterns in the simulated scalar time traces is captured

* *Corresponding author address*: Tsutomu Watanabe, Forestry and Forest Products Research Institute, Dept. of Meteorological Environment, P.O.Box16, Tsukuba-Norin, Tsukuba, Ibaraki 305-8687, Japan

Table 1. Setup of the LES runs. Sampling intervals are for the 2D data collections.

Run	I	II	III
$N_x \times N_y \times N_z$	192 × 192 × 81	384 × 384 ×161	192 × 192 × 81
Flow type	Shear-driven (Plane Couette flow)	Shear-driven (Plane Couette flow)	Pressure-driven (Plane channel flow)
Top boundary	No-slip rigid lid	No-slip rigid lid	Free slip rigid lid
Sampling interval (h/U_h)	0.1	0.07	0.1
Sampling period (h/U_h)	500	350	500

by the conditional sampling technique, and a mechanism behind the structures is investigated.

2. METHOD

2.1 Model equations

The basic equations used in the LES are the filtered Navier-Stokes equations under the Boussinesq approximation, the equation of continuity, and the conservation equation for a passive scalar. The effect of buoyancy is neglected to mimic a neutrally stratified flow.

$$\frac{\partial\langle u_i\rangle}{\partial t} = -\frac{\partial\langle u_j\rangle\langle u_i\rangle}{\partial x_j} - \frac{1}{\rho}\frac{\partial\langle p\rangle}{\partial x_i} - \frac{\partial\tau_{ij}}{\partial x_j} - c_d a U\langle u_i\rangle \quad (1)$$

$$\frac{\partial\langle u_i\rangle}{\partial x_i} = 0 \quad (2)$$

$$\frac{\partial\langle\chi\rangle}{\partial t} = -\frac{\partial\langle u_j\rangle\langle\chi\rangle}{\partial x_j} - \frac{\partial\tau_{\chi j}}{\partial x_j} - c_\chi a U\left(\langle\chi\rangle - \chi_c\right) \quad (3)$$

where the angle brackets denote filtered variables; u_i is the velocity in the x_i-direction; p is the pressure; ρ is the air density; χ is the scalar concentration; τ_{ij} and $\tau_{\chi j}$ are the SGS (sub-grid scale or sub-filter scale) fluxes of momentum and the scalar, respectively; c_d and c_χ are the leaf drag coefficient and the scalar exchange coefficient for a leaf, respectively; a is the leaf area density; U is the instantaneous local wind speed [$=(<u_i><u_i>)^{0.5}$], and χ_c is the scalar concentration at a leaf surface. The final terms in Eqs. (1) and (3) represent the sink or source of momentum and the scalar due to canopy elements, respectively.

The SGS fluxes in Eqs. (1)–(3) are parameterized using resolved-scale variables and the SGS kinetic energy as:

$$\begin{aligned}\tau_{ij} &= \langle u_i u_j\rangle - \langle u_i\rangle\langle u_j\rangle \\ &= -K_m\left(\frac{\partial\langle u_i\rangle}{\partial x_j} + \frac{\partial\langle u_j\rangle}{\partial x_i}\right) + \delta_{ij}\frac{2}{3}\langle e\rangle\end{aligned} \quad (4)$$

$$\tau_{\chi j} = \langle\chi u_j\rangle - \langle\chi\rangle\langle u_j\rangle = -K_\chi\frac{\partial\langle\chi\rangle}{\partial x_j} \quad (5)$$

$$K_m = c_k L\langle e\rangle^{1/2} \quad (6)$$

$$K_\chi = K_m / S_c \quad (7)$$

where e is the SGS kinetic energy; K_m and K_χ are the SGS eddy diffusivities for momentum and the scalar, respectively; c_k is a model constant (=0.07); δ_{ij} is the Kronecker delta; L is the SGS length scale; and S_c is the SGS Schmidt number (=1/3). As in previous LES studies (e.g., Moeng, 1984; Shaw and Schumann, 1992; Kanda and Hino, 1994; Su et al., 1998; Patton et al., 1998), the SGS kinetic energy is predicted by the following equation:

$$\begin{aligned}\frac{\partial\langle e\rangle}{\partial t} = &-\frac{\partial\langle u_j\rangle\langle e\rangle}{\partial x_j} - \tau_{ij}\frac{\partial\langle u_i\rangle}{\partial x_j} + \frac{\partial}{\partial x_j}\left(2K_m\frac{\partial\langle e\rangle}{\partial x_j}\right) \\ &- c_\varepsilon\frac{\langle e\rangle^{3/2}}{L} - 2c_d a U\langle e\rangle\end{aligned} \quad (8)$$

where c_ε is a model constant (=0.93) for viscous dissipation. For the evaluation of model constants, see Watanabe (2004).

2.2 Simulation setup

Three LES runs were conducted with different configurations of the basic flow. Run I and Run II were shear-driven flows in small and large domains, respectively; while Run III was a pressure-driven flow in a small domain. The numbers of grid points in the streamwise (N_x), spanwise (N_y) and vertical (N_z) directions used in each run are given in Table 1. For all runs, the grid interval was uniformly set at $0.1h$ in all directions, with h being the canopy height. The lateral boundaries were periodic. At the bottom boundary, the SGS fluxes were evaluated from resolved variables at the lowest level, with the prescribed roughness lengths for momentum and the scalar assuming instantaneous logarithmic profiles near the ground surface. A constant longitudinal wind velocity was imposed at the top boundary for Runs I and II, while an external longitudinal pressure-gradient was given independent of time and space in Run III. The SGS fluxes at the top boundary were evaluated in the same manner as at the interior grid points for Runs I and II, but were set at zero (free-slip) for Run III. In all three runs, a constant scalar concentration χ_{top} was imposed at the top boundary, and a different constant value χ_c was assumed for the scalar concentration at all leaf and

ground surfaces. The leaf area density (a) was homogeneously distributed within the canopy layer. These specifications realized ideal simulations with complete homogeneity except for the contrast between the canopy layer and the atmospheric layer above it. All equations were then non-dimensionalized using U_h, (χ_{top}–χ_c) and h, where U_h is the mean wind speed at the canopy top.

A pseudo-spectral method was used to evaluate the horizontal derivatives, and a fourth-order compact finite-differencing scheme (Lele, 1992) was used to approximate the vertical derivatives. The time integration was performed using a third-order Runge–Kutta method (Williamson, 1980). The instantaneous pressure field was evaluated from a Poisson equation in spectral space. To eliminate aliasing errors, the Fourier modes of the top one third of the admissible wavenumbers were truncated at every time step (Orszag, 1971). Thus, the effective grid spacing was 1.5 times larger than the original grid interval in the physical domain. The SGS length scale was estimated as:

$$L = \left(1.5\Delta x \cdot 1.5\Delta y \cdot \Delta z\right)^{1/3}. \tag{9}$$

The resolved variables were initialized with horizontally homogeneous vertical profiles as:

$$\frac{\langle u \rangle}{U_h} = \frac{\langle \chi \rangle - \chi_c}{\chi_{top} - \chi_c} = \begin{cases} 1, & z > h; \\ 0.2, & z \le h, \end{cases} \tag{10a}$$

$$\langle v \rangle = \langle w \rangle = 0. \tag{10b}$$

For the velocity field alone, a small degree of random noise was superimposed on this uniform profile to initiate three-dimensional motion. To ensure stable computations, a short time step was used for the initial 20,000 steps, and afterward it was increased as much as possible under the constraint of numerical stability (but kept constant throughout each run). In all runs, spin-up runs were initially performed until the turbulence statistics indicated a quasi-steady state; thereafter, the data collection runs were started.

During the data collection runs, 100 sets of three-dimensional outputs were stored at even time intervals. Two-dimensional data on horizontal (x–y) and vertical (x–z and y–z) slices of the domain were sampled 5,000 times during the same period. The sampling interval and the sampling period for each run are shown in Table 1. In what follows, a horizontal mean value is denoted with brackets [ ] and a departure from the horizontal mean is shown with double primes (″). Similarly, an overbar ($\bar{}$) and a single prime (′) denote time-averaged values and fluctuations, respectively. All variables will be shown normalized using U_h, (χ_h–χ_c) and h unless otherwise mentioned, where χ_h denotes the mean scalar concentration calculated at the canopy height.

2.3 Conditional sampling

Following the approach of Collineau and Brunet (1993a,b) and Lu and Fitzjarrald (1994), a wavelet analysis of the scalar time traces was used to detect the ramp signals. The wavelet transform of a time trace $\chi(t)$ can be written as:

$$T_p\left(a_w, b_w\right) = \frac{1}{a_w}\int_0^T g\left(\frac{t - b_w}{a_w}\right)\chi(t)dt, \tag{11}$$

where g represents a wavelet function, a_w is the time scale of the wavelet, b_w is the center of the wavelet, and T is the recording time. The wavelet variance (V_w) is defined as:

$$V_w\left(a_w\right) = \int_0^T T_p\left(a_w, b_w\right)^2 db_w. \tag{12}$$

A Haar function was adopted as the wavelet function:

$$g_{a,b}(t) = \begin{cases} +1 & \text{for} \quad t \in \left[b_w - a_w/2, b_w\right]; \\ -1 & \text{for} \quad t \in \left[b_w, b_w + a_w/2\right]; \\ 0 & \text{otherwise.} \end{cases} \tag{13}$$

Since the wavelet transform using a Haar function takes a large positive (negative) value when a sudden drop (jump) is observed in the original time trace, it provides a good indicator of ramp patterns.

To enable an 'average' spatial structure to be captured, the conditional sampling of ramp patterns was performed at numerous grid points located just above the canopy, and instantaneous turbulence variables in the space around the detected positions were gathered to make composite figures. The detailed procedures were as follows:

1. Performing the wavelet transform at various time scales for the scalar time-traces recorded at all grid points on a cross-stream transect line just above the canopy;
2. Determining the representative time scale a_0 as the peak of the wavelet variance averaged over the transect line;
3. Performing the wavelet transform at the scale a_0 for the scalar-time traces recorded at all grid points in the two horizontal transect lines (streamwise and cross-stream) that cross the center of the horizontal surface just above the canopy;
4. Detecting as the ramp events the time when the wavelet transform took local minima smaller than a given threshold value;
5. Compositing the spatial distributions of all instantaneous variables around the detected points.

3. RESULTS

Unless otherwise mentioned, the results presented in the following sections are generally from Run I, while some results from other runs are shown for comparison.

3.1 Spectra and turbulence length scales

Streamwise one-dimensional spectra were obtained by firstly performing a two-dimensional Fourier transform in the horizontal plane, and by secondly integrating with respect to cross-stream

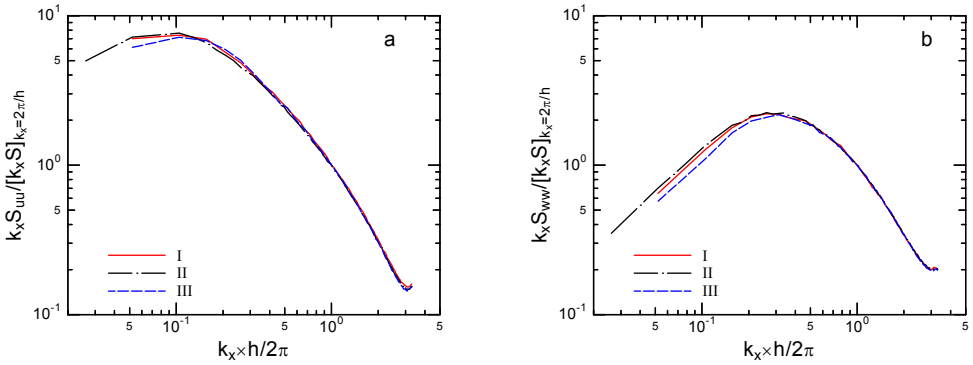

Figure 1. Normalized energy spectra obtained at the height of the canopy top, plotted as functions of the normalized streamwise wavenumber: (a) u; (b) w.

wavenumbers. The spectra were finally averaged over time. Figures 1a and 1b show the one-dimensional energy spectra for streamwise and vertical velocities at the height of canopy top, respectively. These spectra are plotted normalized with respect to their own values at a streamwise wavenumber of $k_x = 2\pi/h$ in the inertial subrange. Spectra are almost independent of the flow type and the domain size. Spectral peaks are found at around $k_x h/2\pi$ = 0.1 and 0.3 for streamwise and vertical velocities, respectively.

As shown by Raupach et al. (1996), the streamwise spacing (Λ_x) between dominant canopy eddies observed in fields and wind-tunnels is well represented by a linear relationship: $\Lambda_x = 8.1 L_s$, where L_s is a length scale of the wind shear across the canopy top, defined as $L_s = U_h/(dU/dz)_{z=h}$. This relationship can be used to test the realism of simulated turbulence field. Since the shear length scale in the simulated flows was approximately the same for all of the present runs as $L_s = 0.41h$, the mixing-layer analogy predicts that the eddy spacing should be $\Lambda_x = 3.32h$ in all runs.

To compare with this prediction, the spectral length scale (Λ_p) is estimated from the peak wavenumbers (k_p) of the energy spectra of vertical velocity. As shown above, the peak wavenumber was k_x = $0.3 \times 2\pi/h$; hence $\Lambda_p = 2\pi/k_p \sim 3.3h$. Another length scale can be derived from the two-point correlation function between vertical velocities at two different points separated in the streamwise direction at the canopy top, i.e.,

$$\Lambda_c = 2\pi \int_0^\infty r_{ww}(r_x, 0, h)\, dr_x \,, \tag{14}$$

where Λ_c is the two-point length scale and r_{ww} is the horizontal two-point correlation function of vertical velocity, defined as:

$$r_{ww}(r_x, r_y, z) = \frac{\left[w''(x + r_x, y + r_y, z, t)\, w''(x, y, z, t)\right]}{\sigma_w^2(z)} \tag{15}$$

where r_x and r_y are horizontal distances in the streamwise and spanwise directions, respectively, and

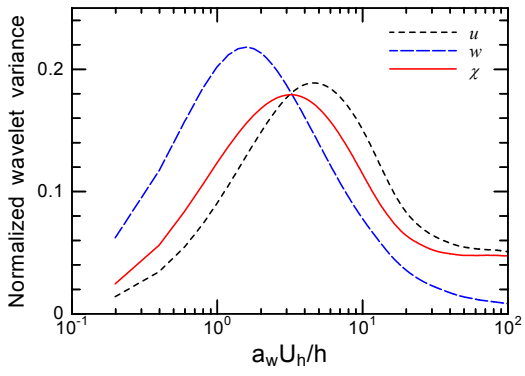

Figure 2. Wavelet variance scalogram calculated from the turbulence time traces simulated just above the canopy.

Table 2. Normalized time scale of the peak of wavelet variance (= $a_0\, U_h/h$)

Run	I	II	III
Streamwise velocity	4.6	5.3	4.5
Vertical velocity	1.6	1.7	1.6
Scalar concentration	3.2	3.2	3.1

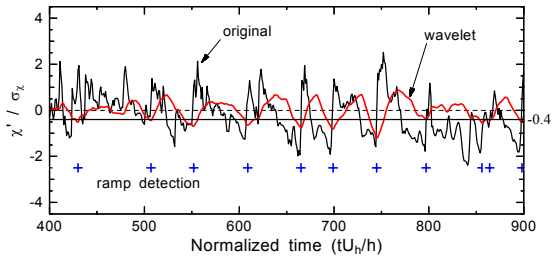

Figure 3. A sample of ramp detections (cross plots) using the wavelet transform (red line) of the original scalar time trace (black line). The horizontal solid line indicates the threshold of detection.

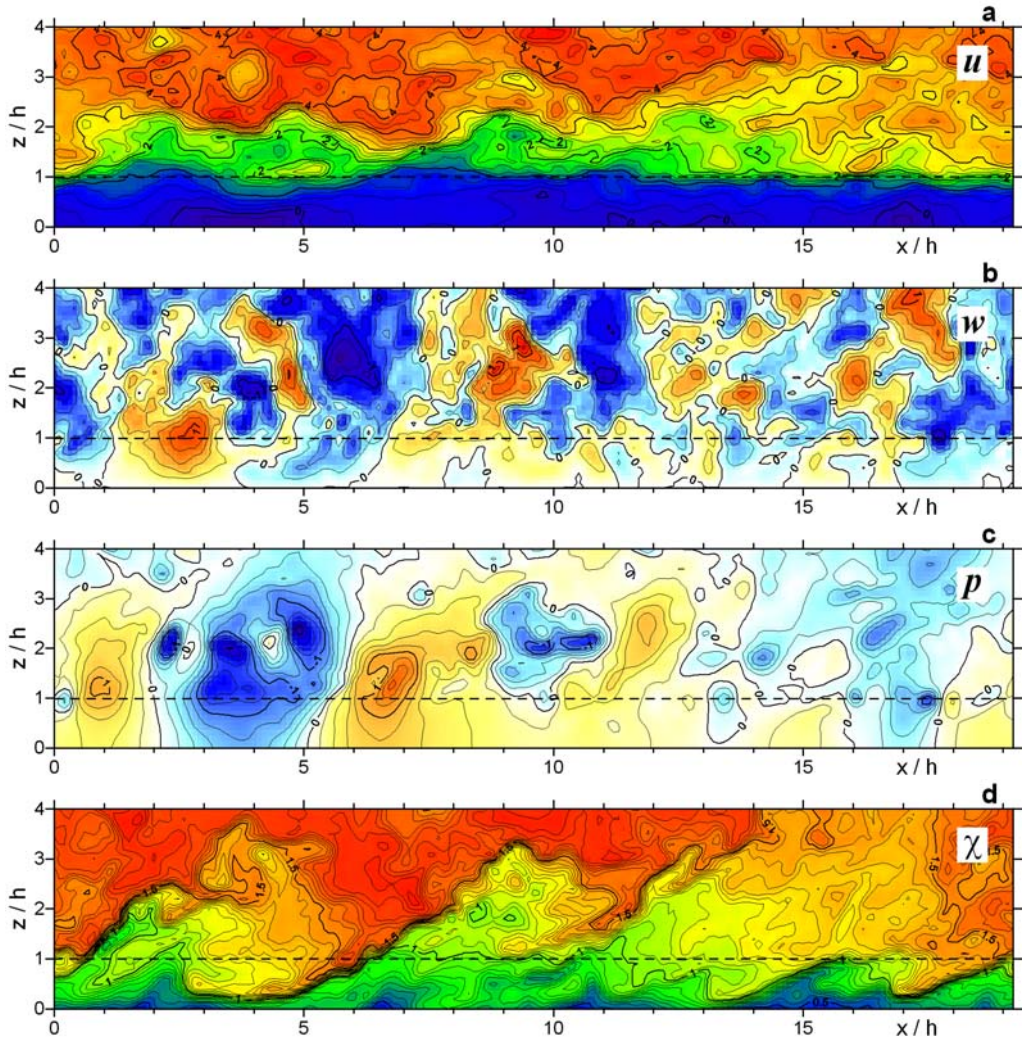

Figure 4. Contours of instantaneous flow variables in the x–z plane in the middle of the computational domain: (a) u/U_h; (b) w/U_h; (c) p/U_h^2; (d) $(\chi-\chi_c)/(\chi_h-\chi_c)$. The contour intervals are (a) 0.25, (b) 0.2, (c) 0.2 and (d) 0.05. Red (blue) color indicates lager (smaller) values for (a) and (d), and positive (negative) values for (b) and (c).

σ_w is the standard deviation of the vertical velocity. The resulting length scales are $\Lambda_c = 3.46h$, $3.64h$ and $3.20h$ for Runs I, II and III, respectively.

Thus, by the reasonable consistency found between these predicted and calculated length scales, it is evident that the present simulations produced quite realistic turbulence fields, where variations in the vertical velocity near the canopy top are caused by a mechanism analogous to the mixing-layer turbulence, associated with the inflected wind profile.

3.2 Ramp detection

Wavelet transform of the scalar time trace was first performed at all grid points in a cross-stream transect. The resulting wavelet variances were then normalized by the time variances at each point and averaged along the transect line. Figure 2 shows the resulting scalogram for the wavelet variance of u, w and χ. The normalized time scales of the scalogram peak are $a_0U_h/h = 4.6$, 1.6 and 3.2 for u, w and χ, respectively, and those from other runs are listed in Table 2. For all of the present runs, the peak time scales are longest for u, shortest for w and intermediate for χ, the order being consistent with field observations in a pine forest (Collineau and Brunet, 1993b). These values are used as the representative time scale in the detection of ramp patterns. Setting the threshold value at –0.4 times the standard deviation of each time trace, as was done by Lu and Fitzjarrald (1994), allows the wavelet transform to provide a reasonably good detection of ramps, as

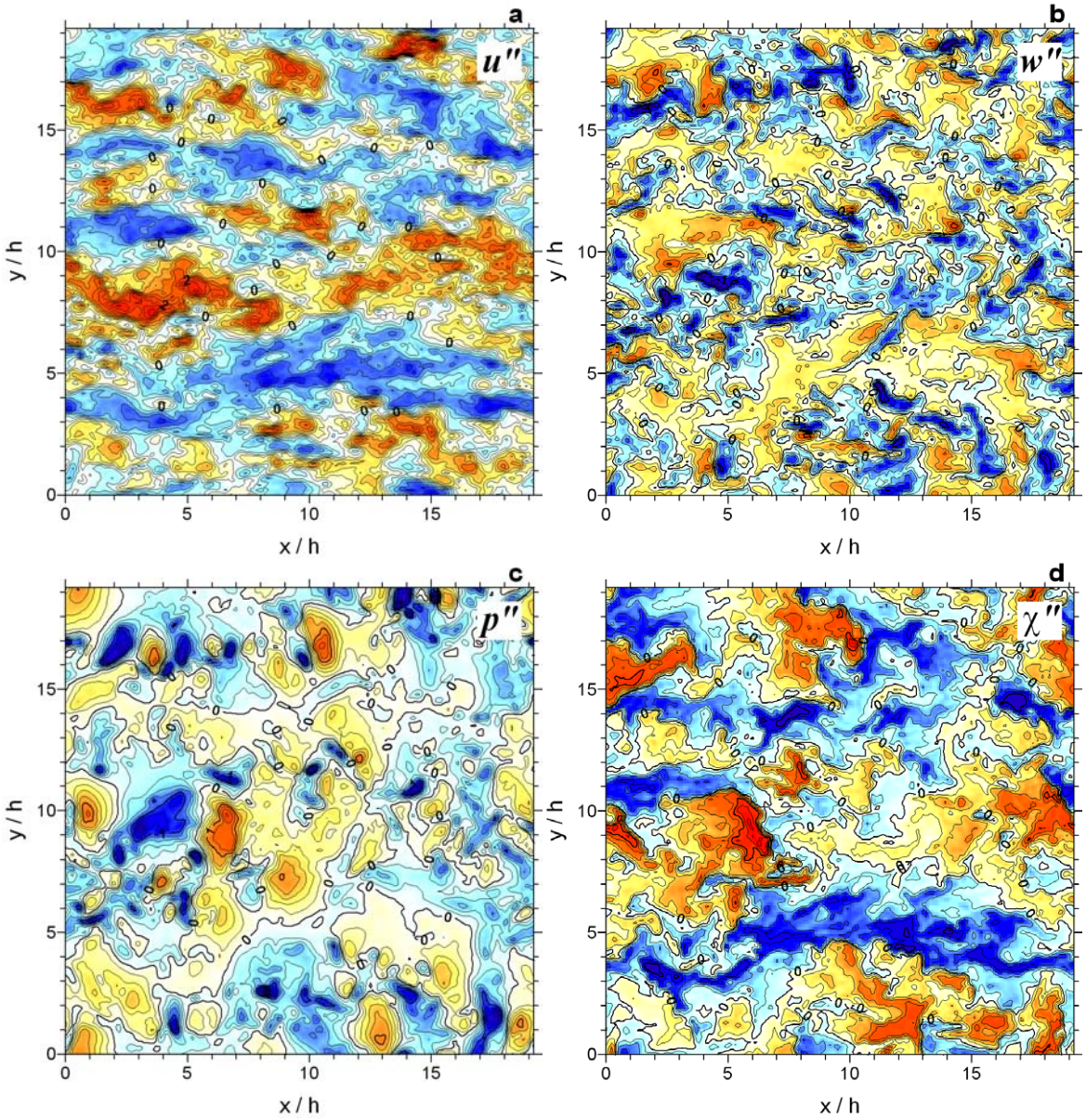

Figure 5. Contours of instantaneous flow variables in the x–y plane just above the canopy: (a) u''/U_h; (b) w''/U_h; (c) p''/U_h^2; (d) $\chi''/(\chi_h–\chi_c)$. The contour intervals are (a) 0.25, (b) 0.2, (c) 0.2 and (d) 0.1. Red and blue colors indicate positive and negative values, respectively.

shown in Figure 3.

3.3 Instantaneous spatial patterns

Figures 4a–d are examples of instantaneous spatial distributions of turbulence variables in a streamwise–vertical slice of the lower half of the computational domain. It is clear from the first two figures that the areas of large streamwise velocity (Figure 4a) correspond to downdraft areas (Figure 4b). Several microfrontal structures are seen in the distribution of the scalar concentration in Figure 4d. The largest microfront, associated with the most coherent downdraft area (x/h = 5–7), extends from near the bottom of the canopy to three times the canopy height. All the microfronts tilt downstream. The distribution pattern of kinematic pressure (Figure 4c) is much smoother than that of the other variables, provably because of its non-local characteristics. Generally, an intensively low pressure in a flow is known to indicate existence of vortices (e.g., Lin et al., 1996). Indeed, in Figure 4c, pressure minima are

found coinciding with both the large vertical shears of streamwise velocity in Figure 4a and paired downstream downdrafts and upstream updrafts in Figure 4b. These vortex signatures are seen between the scalar microfronts. The locations of high-pressure areas, on the other hand, are identical to those of the scalar microfronts.

Figure 5 shows the instantaneous horizontal distributions just above the canopy at the same moment as the images in Figure 4. The correlation between large streamwise velocities (Figure 5a) and negative vertical velocities (Figure 5b) is obvious once again. This correlation is also seen between the positive perturbations of the scalar concentration (Figure 5d) and the negative vertical velocities. However, the streamwise velocity exhibits more elongated patterns than the scalar. Elongated regions of low-speed and high-speed velocities alternate with one another in the lateral and/or streamwise directions. An animation of these results showed that these elongated patterns never disappeared in the simulation period although they meandered and moved with time. Since elongated structures of similar lateral spacing were also observed in Runs II and III (not shown), these elongated structures are not artifacts due to the limitation of domain size or an influence of the imposed top-boundary velocity.

The contours of vertical velocity include finer structures (Figure 5b). Roughly speaking, the horizontal scales of intensive negative spots (dark blue area) are less than 1*h* in width and less than 3*h* in length. However, as we saw in Figure 4b, downdrafts generally have substantial horizontal scales well above the canopy. Hence, these fine-grained structures are produced near the canopy top, probably by the inflection instability mechanism discussed previously. This issue will be revisited later. The more important point that should now be noted in Figure 5b is that these individual downdraft spots do not directly correspond to the scalar microfronts in Figure 5d, but the front lines of the downdraft envelopes, which include several intensive downdraft spots therein, do correspond.

In contrast with the spot-like distribution of downdrafts, updrafts occupy wider areas with fewer broad peaks. The combination of strong and narrow downdrafts with weak and broad updrafts explains the observations of negative skewness of the vertical velocity within plant canopies (e.g., Raupach et al., 1996). Small-scale structures in the pressure pattern (Figure 5c) are concentrated in the regions of high-speed streamwise velocity. High-pressure areas coincide with the scalar microfronts, while intense low-pressure spots lie inside the paired updrafts and downdrafts, indicating the existence of vortices.

3.4 Averaged eddy structure

In the followings, results are shown for averaged spatial structures of organized turbulence that cause significant ramp patterns in the scalar time traces. The structures will be presented as deviations from the horizontal mean values at each height, being normalized with respect to U_h and $(\chi_h - \chi_c)$.

3.4.1 Vertical–streamwise cross-sections

The x–z cross-sections of averaged fields of streamwise and vertical velocities, kinematic pressure, and scalar concentration (Figures 6a–d) clearly illustrate that the scalar ramps observed just above the canopy are the signatures of the passage of the scalar microfront, which is associated with an ejection–sweep structure in the streamwise and vertical velocities and a positive pressure perturbation. The averaged scalar microfront extends from near the ground to up to twice the canopy height, with the largest horizontal gradient just above the canopy. The velocity front is almost coincident with the scalar microfront, but the gradient across the front is more gradual (Compare the horizontal distances between the positive and negative peaks). In contrast with the inclined structures in the streamwise velocity and the scalar, the vertical velocity and pressure exhibit vertically coherent structures.

Gao et al. (1989), who analyzed time–height cross-sections of the ramp events above a deciduous forest, abstracted these author's results as: *Near the top of the forest they are composed of a weak ejecting motion transporting warm and/or moist air out of the forest followed by strong sweeps of cool and/or dry air penetrating into the canopy. The sweep is separated from the ejecting air by a sharp scalar microfront. At approximately twice the height of the forest, ejections and sweeps are of about equal strength*. These descriptions surprisingly fit to the present results.

Large pressure gradients, seen on the both sides of the vertically coherent pressure ridge (Figure 6c), tend to reduce the streamwise gradient of the streamwise velocity across the microfront. Similarly, the lifted updraft region corresponds to the region of a vertical pressure gradient above the pressure maximum. Figure 6c also shows that a region of negative pressure is formed in the upstream of the pressure ridge, indicating that vortex motions are more likely to exist in the upstream of the microfront than in its downstream.

3.4.2 Cross-stream vertical cross-sections

Figure 7 illustrates the spanwise symmetry in the y–z slice of the averaged structures. This does not indicate that individual eddy motions are symmetric. Rather, it resulted from the ensemble averaging along the homogeneous direction. On average, however, the scalar ramp at the height of canopy top is associated with a spanwise divergent flow, a weak downdraft, a broad positive pressure peak, and a sharp vertical gradient in the scalar. There are no significant structures in the negative pressure region, indicating that streamwise vortices, which might induce the spanwise flow pattern shown here, are unlikely. Instead, the spanwise divergent flow coincides with the region of the spanwise pressure gradient. The flow

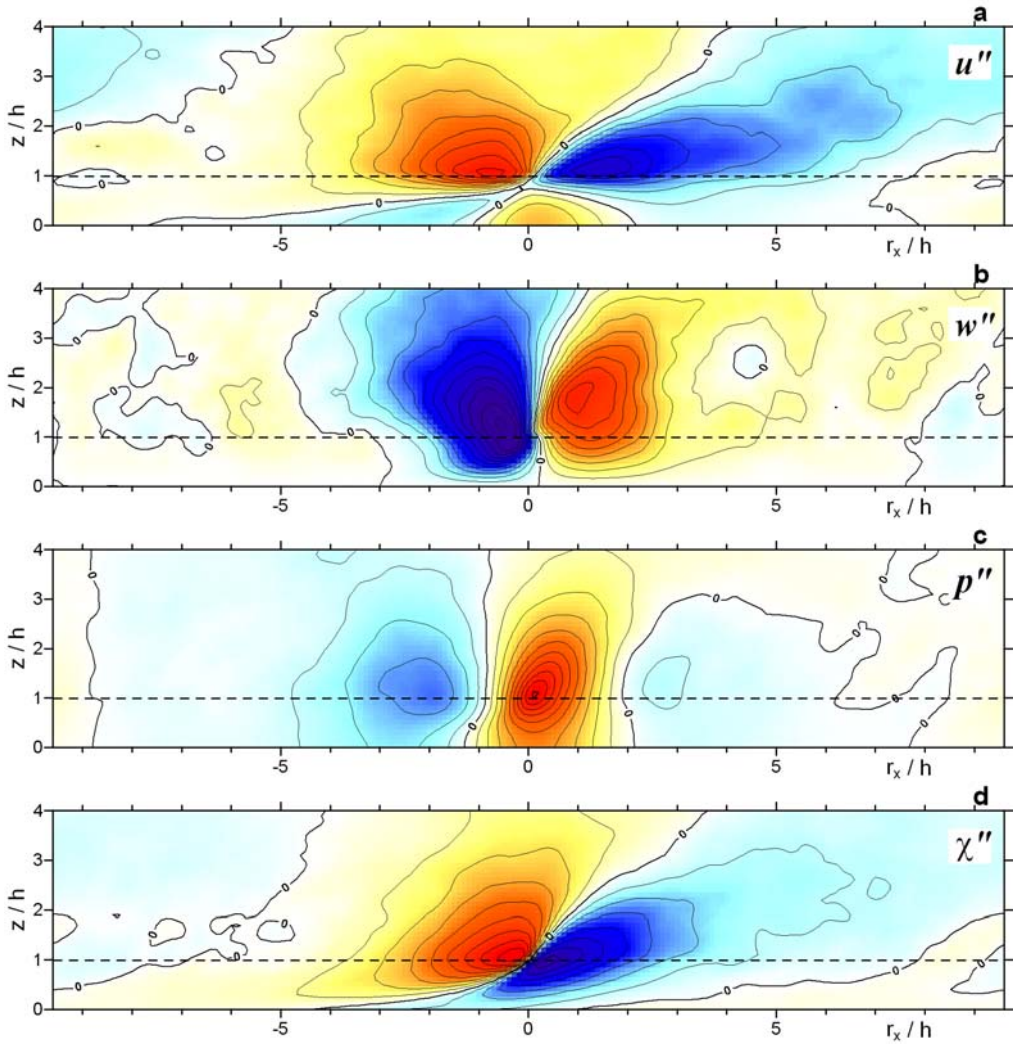

Figure 6. Contours of flow variables in the x–z slice of the ensemble-averaged eddy structure: (a) u''/U_h; (b) w''/U_h; (c) p''/U_h^2; (d) $\chi''/(\chi_h-\chi_c)$, with contour intervals of (a) 0.05, (b) 0.025, (c) 0.05 and (d) 0.025. Red and blue colors indicate positive and negative values, respectively. r_x denotes the streamwise distances from the ramp-detection location.

patterns in both the x–z and the y–z cross-sections suggest that the positive pressure ridge is due to the streamwise (quasi-) stagnation that forms at the downstream end of high-speed downdrafts (sweeps).

Overall, the vertical structures presented in Figures 6 and 7 are quite similar to the characteristic eddy presented by Finnigan and Shaw (2000). These authors depicted the flow pattern in the characteristic eddy as follows: (1) an ejection is followed by a sweep, with maximum velocities observed slightly above the canopy; (2) the sweep is more streamwise localized beneath the canopy than just above the canopy; (3) the sweep is followed by a region of non-coherent flow; and (4) the downsweep is confined to a spanwise-narrow region and penetrates only the upper third of the canopy before spreading sideways. All these depictions also apply to the present averaged results.

3.7.3 Horizontal cross-sections

Figures 8a to 8e show the horizontal slices at the canopy height of the averaged structures. These figures indicate that a distinct scalar ramp generally occurs at a point where an elongated region of high-speed streamwise velocity overtakes another elongated region of low-speed velocity. Both the spanwise divergent flow and the spanwise coherent positive-pressure region formed at the ramp location suggest a streamwise stagnation due to the impact of the high-speed and low-speed regions. A region of spanwise convergent flow, which is also elongated,

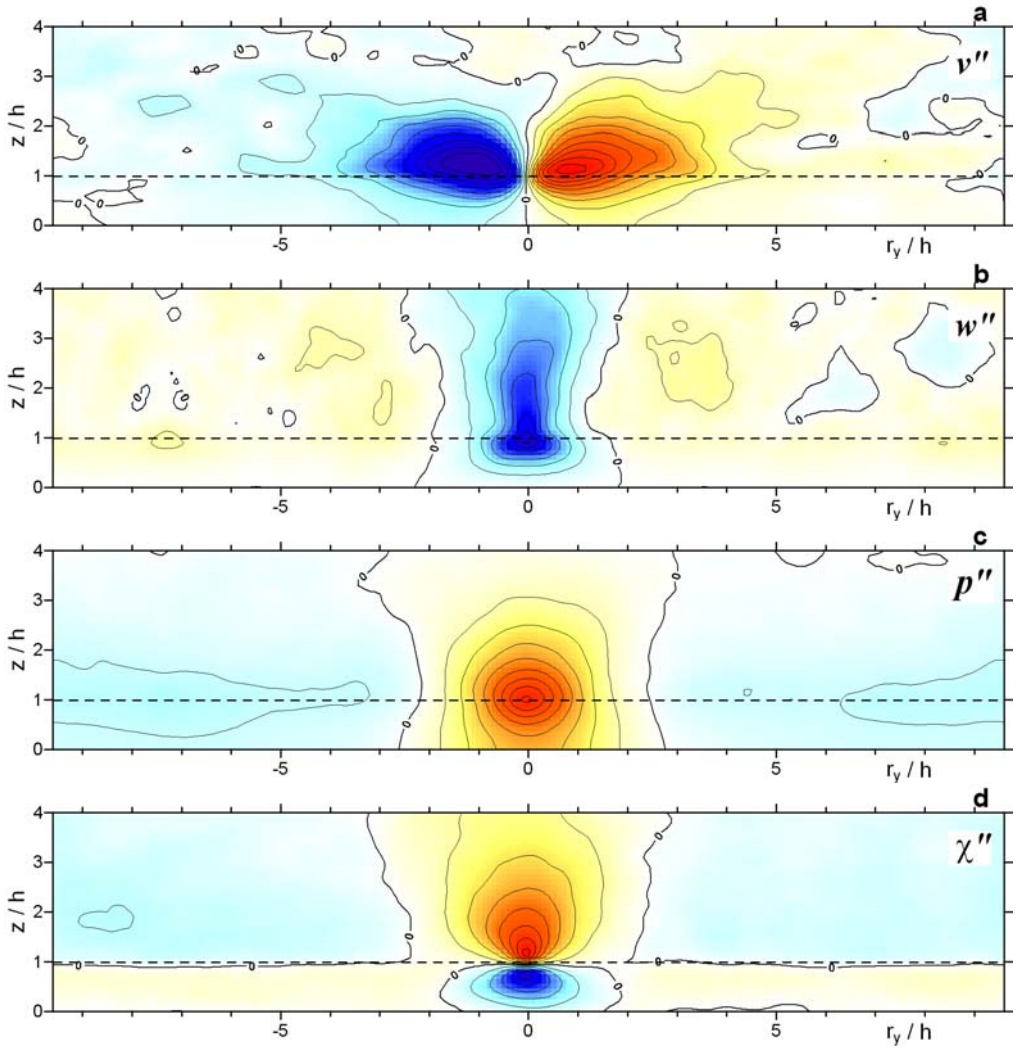

Figure 7. Contours of flow variables in the y–z slice of the ensemble-averaged eddy structure: (a) v''/U_h; (b) w''/U_h; (c) p''/U_h^2; (d) $\chi''/(\chi_h-\chi_c)$, with contour intervals of (a) 0.025, (b) 0.025, (c) 0.05 and (d) 0.025. Red and blue colors indicate positive and negative values, respectively. r_y denotes the cross-stream distances from the ramp-detection location.

appears downstream of the ramp. Such elongation is not observed in the distribution of vertical velocity at the canopy top. However, as we saw in Figure 6b, the downdraft of this averaged structure is more extended in the streamwise direction at higher levels than that at the canopy top.

4. DISCUSSION

4.1 Comparison with mixing-layer analogy

As shown earlier, the mixing-layer analogy predicts the streamwise spacing of dominant canopy eddies as $\Lambda_x = 3.32h$ for the present simulations. However, the horizontal scale of the updraft–downdraft pair in the averaged structure is more than six times the canopy height (Figure 6b). Since the size of eddies should be smaller than the spacing between them, the horizontal scale of the averaged structure is much larger than that of canopy eddies expected from the mixing-layer analogy. The structures obtained for the vertical velocity and pressure are also much taller than the shear length scale of $0.41h$ (Figures 6b, 6c, 7b and 7c). Moreover, the horizontal patterns for the streamwise velocity of the averaged structure are elongated in the streamwise direction, total length being more than $10h$. Therefore, the averaged structure is not attributable to an eddy motion arising from the canopy-top inflection instability.

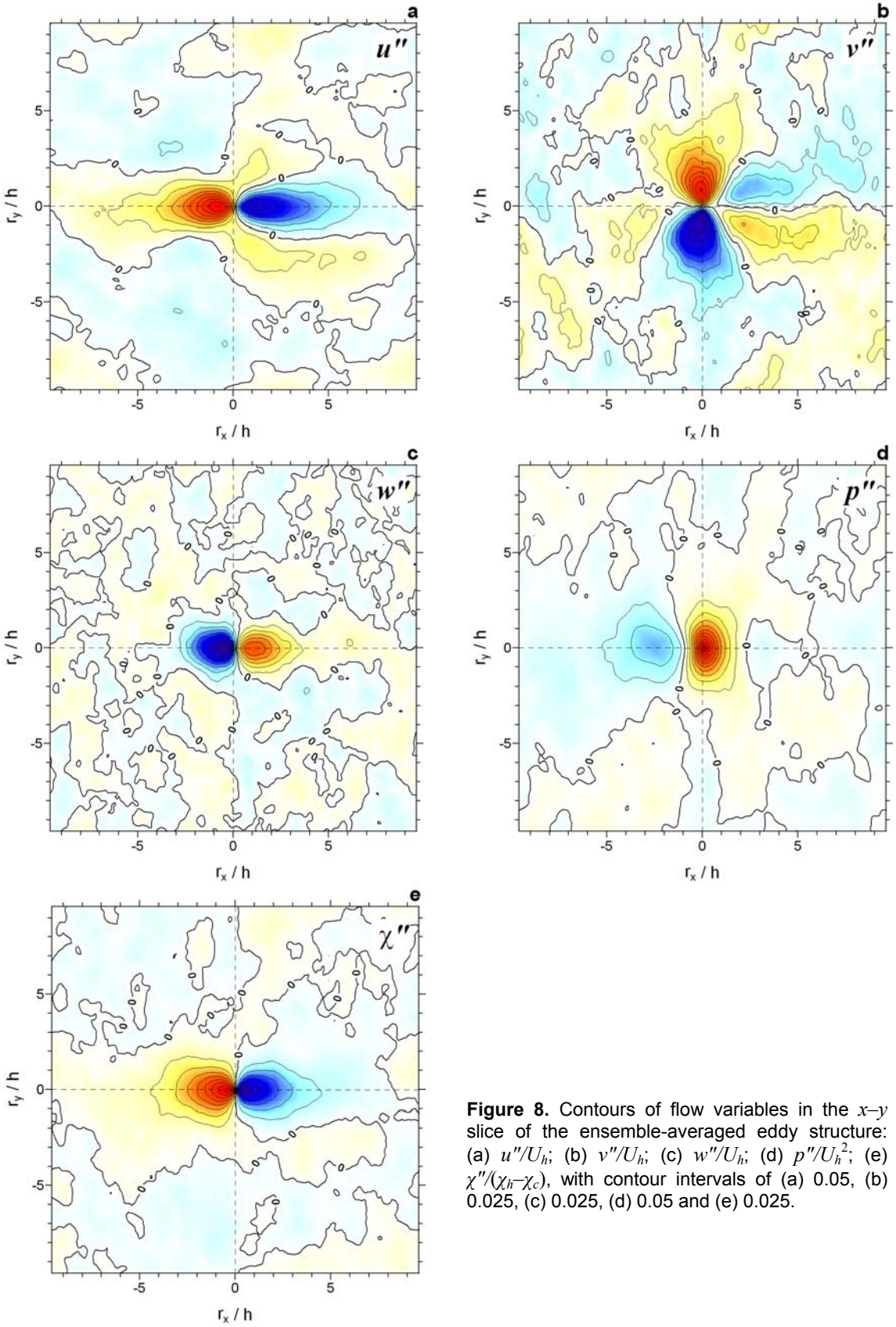

Figure 8. Contours of flow variables in the x–y slice of the ensemble-averaged eddy structure: (a) u''/U_h; (b) v''/U_h; (c) w''/U_h; (d) p''/U_h^2; (e) $\chi''/(\chi_h-\chi_c)$, with contour intervals of (a) 0.05, (b) 0.025, (c) 0.025, (d) 0.05 and (e) 0.025.

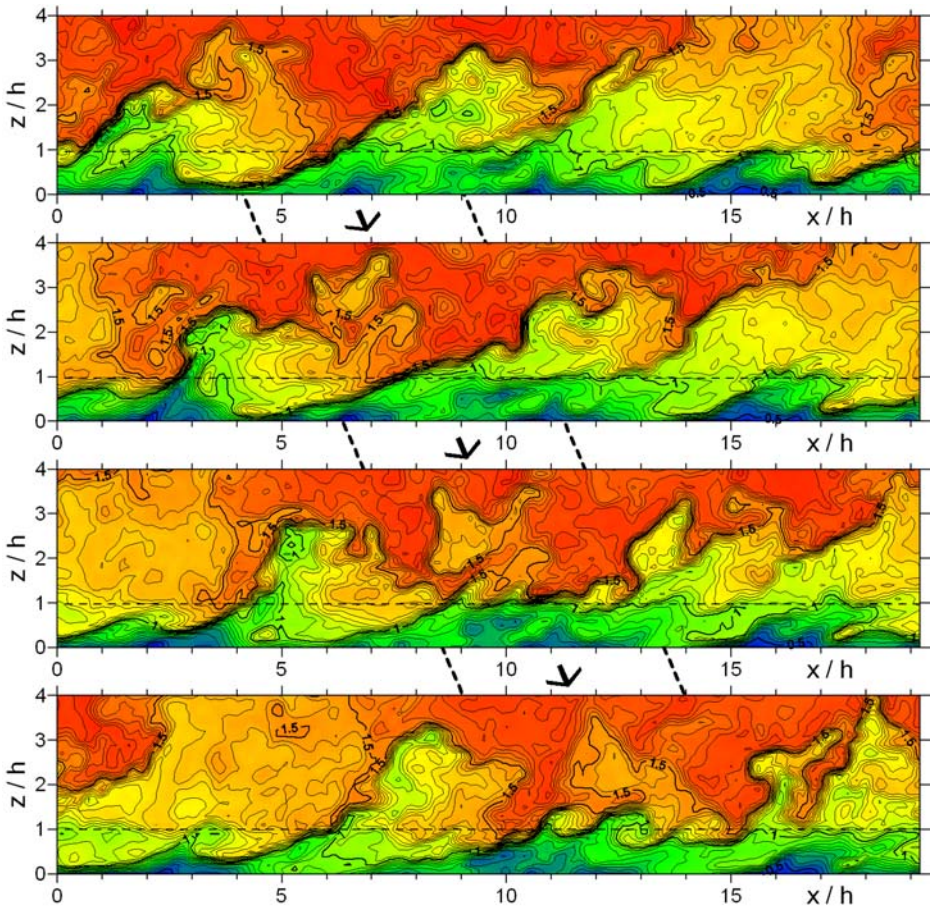

Figure 9. Time sequence of the instantaneous scalar contours in the x–z plane. The time interval between panels is $0.8\ h/U_h$. The broken lines and arrows drawn between the panels indicate the movement of a coherent downdraft. Three K–H patterns appear across the canopy top in $11 < x/h < 15$ in the bottom panel.

Although not shown here, the averaged structures obtained from Runs II and III were essentially similar to that obtained from Run I. The spatial scales of the vertical patterns in these runs were far larger than the shear length scale. The horizontal structures in the streamwise velocity were elongated also in Runs II and III; and the spanwise width of the structures was comparable to that shown in Figure 8a. Thus, the obtained structures should not be considered to be false images projected by the computational configurations. There must be a common inherent mechanism for creating these large structures. Since the most remarkable feature appearing in common in all runs was the strongly-sheared wind profile just above the canopy, this may be involved in the mechanism. This raises an analogy to the streak structures (or the streak-induced eddies), which were discussed in Introduction.

4.2 Mechanism of scalar microfronts

From these results, it can be inferred that a distinct scalar microfront develops where a coherent downdraft associated with a high-speed streak penetrates into a low-speed area associated with updrafts. The flow stagnation formed at the leading head of the high-speed downdraft builds up a vertically-coherent high-pressure region at the same position. The pressure gradients around this high-pressure region tend to reduce the streamwise gradients of streamwise velocity and to enhance spanwise divergent flows and lifted updrafts downstream from the microfront, thereby satisfying the constraint of continuity.

The analysis of turbulence length scales presented in section 3.1 indicates that variations in the vertical velocity near the canopy top are primarily due to canopy-scale eddies produced by the inflection instability. However, since the spatial scales of the averaged structures are much larger than the shear length scale, the canopy-scale eddies may not be the main causal mechanism for the microfronts or ramp patterns of significant strength. Rather, the canopy-scale eddies are produced most often when

the coherent high-speed downdraft impinges on the canopy, with the leading head of the downdraft producing the microfront.

To confirm this view, one such realization is demonstrated in Figure 9, which shows a time sequence of the distribution of the scalar concentration in a vertical–streamwise slice, subsequent to the snapshot shown in Figure 4d. The broken lines and arrows drawn between panels indicate the movement of a large-scale mother downdraft. As time advanced, the downstream-tilted microfront seen in the top panel became more and more parallel to the canopy surface, implying an enhancement of the shear instability across the canopy top. Thereafter, small-scale Kelvin–Helmholtz patterns started to develop near the canopy top, and three well-developed patterns appeared in the region of the mother downdraft, as shown in the bottom panel. This view is consistent with Finnigan's (1979) field observation that *honami* or canopy-scale sweeps tend to arrive over wheat canopies in trains of 3 or 4 over a well-defined period. However, the present result implies that each sweep may not necessarily be associated with a scalar ramp of significant strength.

5. CONCLUSIONS

Turbulence characteristics produced by the present LES were fairly consistent with the well-accepted previous observations on the nature of canopy turbulence. Among others, the turbulent length scales defined for the vertical velocity, one derived from the peak wavenumber of the energy spectrum and the other from the spatial correlation function, both agreed with the prediction by the mixing-layer analogy of Raupach et al. (1996).

The conditional sampling triggered by wavelet-based ramp detections permitted an inspection of the 'average' eddy structure that causes the scalar ramp signals. The vertical slices of the averaged structure indicated that the scalar ramps are caused by the passage of the scalar microfrons, which are associated with the ejection–sweep structure of the streamwise and vertical velocities, the spanwise divergent flow near the canopy top, and a vertically-coherent, positive pressure perturbation. These characteristics are also consistent with the results of previous measurements in fields and wind tunnels.

However, the horizontal slice of the averaged structure revealed that this structure represents the moment when a streamwise-elongated region of high-speed streamwise velocity overtakes another elongated region of low-speed velocity. These elongated regions, which resemble the streak structures commonly observed in near-wall shear layers, are of much larger scale than the canopy height and are presumably developed under the influence of a strong shear formed above the canopy. As predicted by the mixing-layer analogy, the canopy-scale eddies indeed dominate the variation in the vertical velocity near the canopy top. But canopy-scale eddies are not directly involved in the formation of the scalar microfront. Rather, these eddies are most often observed in the elongated high-speed region, of which downstream end create the microfront.

The next step of this study would be to investigate whether the streaky structures really exist in the actual canopy flows and, if they do, to clarify the mechanism of such structures.

Acknowledgements

Computations of the present LES were performed on the NEC SX-5B/16Be at the Computer Center for Agriculture, Forestry and Fisheries Research, MAFF, Japan.

References

Bergström, H. and U. Högström, 1989: Turbulent exchange above a pine forest. II. Organized structures. *Boundary-Layer Meteor.*, **49**, 231–263.

Collineau, S. and Y. Brunet, 1993a: Detection of turbulent coherent motions in a forest canopy. Part I: Wavelet analysis. *Boundary-Layer Meteor.*, **65**, 357–379.

Collineau, S. and Y. Brunet, 1993b: Detection of turbulent coherent motions in a forest canopy. Part I: Time-scales and conditional averages. *Boundary-Layer Meteor.*, **66**, 49–73.

Deardorff, J. W., 1970: Numerical investigation of neutral and unstable planetary boundary layers. *J. Atmos. Sci.*, **29**, 91–115.

Drobinski, P., P. Carlotti, R. K. Newsom, R. M. Banta, R. C. Foster and J.-L. Redelsperger, 2004: The structure of the near-neutral atmospheric surface layer. *J. Atmos. Sci.*, **61**, 699–714.

Drobinski, P. and R. C. Foster, 2003: On the origin of near-surface streaks in the neutrally-stratified planetary boundary layer. *Boundary-Layer Meteor.*, **108**, 247–256.

Finnigan, J. J., 1979: Turbulence in waving wheat. II. Structure of momentum transfer. *Boundary-Layer Meteor.*, **16**, 213–236.

Finnigan, J. J., 2000: Turbulence in plant canopies. *Ann. Rev. Fluid Mech.*, **32**, 519–571.

Finnigan, J. J. and R. H. Shaw, 2000: A wind-tunnel study of airflow in waving wheat: An EOF analysis of the structure of the large-eddy motion. *Boundary-Layer Meteor.*, **96**, 211–255.

Foster, R. C., 1997: Structure and energetics of optimal Ekman layer perturbations. *J. Fluid Mech.*, **333**, 97–123.

Gao, W., R. H. Shaw and K. T. Paw U: 1989, 'Observation of organized structure in turbulent flow within and above a forest canopy', *Boundary-Layer Meteorol*. **47**, 349–377.

Kanda, M. and M. Hino, 1994: Organized structures in developing turbulent flow within and above a plant canopy, using a Large-eddy simulation. *Boundary-Layer Meteor.*, **68**, 237–257.

Katul, G. G., C. D. Geron, C.-I. Hsieh, B. Vidakovic and A. B. Guenther, 1998: Active turbulence and scalar transport near the forest–atmosphere

interface. *J. Appl. Meteor.*, **37**, 1533–1546.

Lele, S. K., 1992: Compact finite difference schemes with spectral-like resolution. *J. Comput. Phys.*, **103**, 16–42.

Lin, C.-L., J. C. McWilliams, C.-H. Moeng and P. P. Sullivan, 1996: Coherent structures and dynamics in a neutrally stratified planetary boundary layer flow. *Phys. Fluid*, **8**, 2626–2639.

Lu, C.-H. and D. R. Fitzjarrald, 1994: Seasonal and diurnal variations of coherent structures over a deciduous forest. *Boundary-Layer Meteor.*, **69**, 43–69.

Marshall, B. J., C. J. Wood, B. A. Gardiner and R. E. Belcher, 2002: Conditional sampling of forest canopy gusts. *Boundary-Layer Meteor.*, **102**, 225–251.

Mason, P. J. and D. J. Thomson, 1987: Large-eddy simulations of the neutral-static-stability planetary boundary layer. *Quart. J. Roy. Soc. Meteor.*, **113**, 413–443.

McNaughton, K. G. and Y. Brunet, 2002: Townsend's hypothesis, coherent structures and Monin-Obukhov similarity. *Boundary-Layer Meteor.*, **102**, 161–175.

Moeng, C.-H., 1984: A large-eddy-simulation model for the study of planetary boundary-layer turbulence. *J. Atmos. Sci.*, **41**, 2052–2062.

Moeng, C.-H. and P. P. Sullivan, 1994: A comparison of shear- and buoyancy-driven planetary boundary layer flows. *J. Atmos. Sci.*, **51**, 999–1022.

Orszag, S. A., 1971: On the elimination of aliasing in finite-difference schemes by filtering high-wavenumber components. *J. Atmos. Sci.*, **28**, 1074.

Panton, R. L., 1997: *Self-sustaining mechanisms of wall turbulence*. Computational Mechanics Publications, 422 pp.

Patton, E. G., R. H. Shaw, M. J. Judd and M. R. Raupach, 1998: Large-eddy simulation of windbreak flow. *Boundary-Layer Meteor.*, **87**, 275–306.

Raupach, M. R., J. J. Finnigan and Y. Brunet, 1996: Coherent eddies and turbulence in vegetation canopies: the mixing layer analogy. *Boundary-Layer Meteor.*, **78**, 351–382.

Robinson, S. K., 1991: Coherent motions in the turbulent boundary layer. *Ann. Rev. Fluid Mech.*, **23**, 601–639.

Shaw, R. H. and U. Schumann, 1992: Large-eddy simulation of turbulent flow above and within a forest. *Boundary-Layer Meteor.*, **61**, 47–64.

Su, H.-B., R. H. Shaw, K. T. Paw U, C.-H. Moeng and P. P. Sullivan, 1998: Turbulent statistics of neutrally stratified flow within and above a sparse forest from large-eddy simulation and field observations. *Boundary-Layer Meteor.*, **88**, 363–397.

Watanabe, T., 2004: Large-eddy simulation of coherent turbulence structures associated with scalar ramps over plant canopies. *Boundary-Layer Meteor.*, **112**, 307–341.

Wilczak, J. M. and J. E. Tillman, 1980: The three-dimensional structure of convection in the atmospheric surface layer. *J. Atmos. Sci.*, **37**, 2424–2443.

Williamson, J. H.: 1980, 'Low-storage Runge-Kutta schemes', *J. Comput. Phys.* **35**, 48–56.